

# The full life cycle of a polar low over the Norwegian Sea observed by three research aircraft flights

Ivan Føre,<sup>a\*</sup> Jón Egill Kristjánsson,<sup>a</sup> Øyvind Saetra,<sup>b</sup> Øyvind Breivik,<sup>b</sup> Bjørn Røsting<sup>b</sup> and Melvyn Shapiro<sup>c</sup>

<sup>a</sup>*Department of Geosciences, University of Oslo, Norway*

<sup>b</sup>*The Norwegian Meteorological Institute, Oslo, Norway*

<sup>c</sup>*National Center for Atmospheric Research, Boulder, Colorado, USA*

\*Correspondence to: I. Føre, University of Oslo, Department of Geosciences, P.O. Box 1047, Blindern, Oslo 0316, Norway. E-mail: ifore@geo.uio.no

During 3–4 March 2008, the Norwegian IPY-THORPEX field campaign successfully carried out three flight missions that observed the full life cycle of a polar low over the Norwegian Sea. Here the three-dimensional structure of the polar low has been investigated using dropsonde data from the three flights. The polar low developed in a cold air outbreak, with temperature differences between the sea surface and 500 hPa of about 45–50°C. Cross-sections show that the horizontal gradients of potential temperature weakened as the polar low matured, suggesting that baroclinic energy conversion took place. Dropsonde data of potential temperature and relative humidity show evidence of a tropopause fold, which is possibly a manifestation of upper-level forcing. This is corroborated by potential vorticity inversion, which shows a dominant role of upper-level forcing throughout the polar low's lifetime. During the cyclogenesis stage the polar low circulation was confined below 700 hPa, with a northerly low-level jet of 26 m s<sup>-1</sup>. In the mature stage, its circulation reached up to the tropopause (~450 hPa), with maximum wind speed between 700 and 900 hPa of about 26–28 m s<sup>-1</sup>. At this stage the polar low warm core was about 3 K warmer than surrounding air masses. The deep moist towers at the eye-like structure of the polar low extended up to the tropopause with relative humidity values above 70%, indicating a possibly important role for condensational heating in the development. Estimates of surface fluxes of sensible and latent heat using temperature and moisture from the dropsonde data show latent heat fluxes west of the polar low increasing from 175 to 300 W m<sup>-2</sup> as the low matured, while the sensible heat fluxes rose from 200 to 280 W m<sup>-2</sup>, suggesting a gradually increasing contribution of surface fluxes to the energetics of the polar low with time. Copyright © 2011 Royal Meteorological Society

**Key Words:** research aircraft measurements; PV inversion; IPY-THORPEX; polar lows

*Received 8 November 2010; Revised 14 January 2011; Accepted 16 March 2011; Published online in Wiley Online Library 7 June 2011*

*Citation:* Føre I, Kristjánsson JE, Saetra Ø, Breivik Ø, Røsting B, Shapiro M. 2011. The full life cycle of a polar low over the Norwegian Sea observed by three research aircraft flights. *Q. J. R. Meteorol. Soc.* 137: 1659–1673. DOI:10.1002/qj.825

## 1. Introduction

During recent decades, increased offshore activity in the Nordic Seas has increased the demand for better

forecasts and understanding of adverse weather events such as polar lows. Polar lows are intense and short-lived (<24 hours) mesoscale cyclones (diameter 200–1000 km) with wind speed above gale force frequently observed during

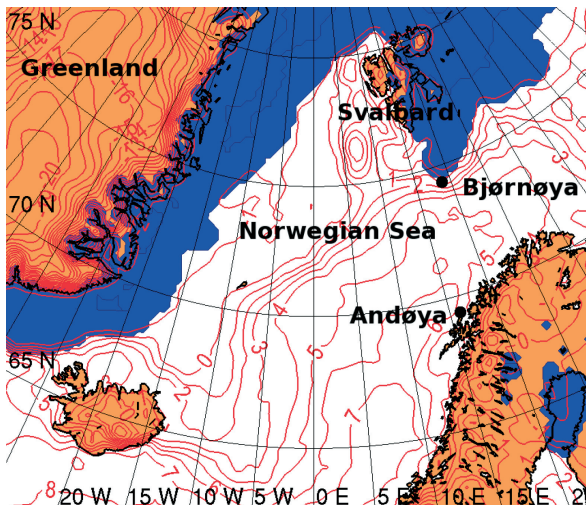


Figure 1. Geographical features, sea-surface temperature ( $^{\circ}\text{C}$ , red contours) and sea ice (blue shading).

wintertime over high-latitude ocean areas (Rasmussen and Turner, 2003). Due to the sparse data coverage of the conventional observational network over the Nordic Seas, polar lows are often poorly predicted and sometimes not even captured at all by weather forecasts. The predictability of polar lows is also limited by the small scale and short lifetime (e.g. Turner *et al.*, 2003). Research aircraft campaigns (Shapiro *et al.*, 1987; Douglas *et al.*, 1991; Brümmer *et al.*, 2009) in combination with numerous numerical simulations (Grønås and Kvamstø, 1995; Bresch *et al.*, 1997; Bracegirdle and Gray, 2008) reveal that polar lows are complex weather systems with a variety of developments, and that several intensification mechanisms can operate simultaneously. Initially polar lows usually develop in a low-level baroclinic environment under the influence of an upper-level potential vorticity (PV) anomaly (Montgomery and Farrell, 1992; Grønås and Kvamstø, 1995). Condensational heating and surface energy fluxes come as additional energy sources (Craig and Gray, 1996; Rasmussen and Turner, 2003).

With the goal of improving weather forecasts and the understanding of severe Arctic weather events such as polar lows, the Norwegian International Polar Year–THe Observing system Research and Predictability EXperiment (IPY–THORPEX) aircraft campaign was launched from Andøya ( $69^{\circ}\text{N}$ ,  $16^{\circ}\text{E}$ , Figure 1), Norway, in February and March 2008 (Kristjánsson *et al.*, 2011). The campaign successfully captured a polar low development that took place over the Norwegian Sea during 3–4 March. For the first time in history three separate flight missions successfully observed the full life cycle of a polar low. Data from dropsondes obtained during this polar low event are the main foundation for this article. The main goal of this article is to give detailed information on the full life cycle and the three-dimensional structure of the polar low by combining dropsonde data with satellite imagery and fields from the operational Norwegian HIRLAM Limited Area Model (HIRLAM: Undén *et al.*, 2002) weather prediction model at the Norwegian Meteorological Institute. In section 2, a short summary of the campaign and the observations is given. A synoptic overview using infrared satellite images (from the US National Oceanic and Atmospheric Administration) and HIRLAM analysis and

forecast products is presented in section 3. This is supported by an inversion of several upper-level PV anomalies in order to quantify the role of upper-level forcing for the polar low development (section 4). In section 5, vertical and horizontal sections of dropsonde data are analysed to give information about the three-dimensional structure of the polar low and to get an insight into its physical properties. Summary and conclusions are presented in section 6.

## 2. Data and analysis

The observations presented in this article were made during the IPY–THORPEX aircraft campaign based at Andøya airport (Figure 1) in northern Norway ( $69^{\circ}\text{N}$ ,  $16^{\circ}\text{E}$ ) in February and March 2008 (Kristjánsson *et al.*, 2011). The Norwegian IPY–THORPEX project is a contribution to the International Polar Year 2007–2008, aiming at improved understanding and forecasting of adverse weather in the Arctic, specifically emphasizing observations of polar lows. During the campaign, 15 flight missions were conducted using the German Aerospace Research Establishment (DLR) Falcon jet aircraft, dropping a total of 150 dropsondes reporting back to the aircraft and further on to the global telecommunication system (GTS). In some cases polar lows were observed in the satellite images but missed by the aircraft. The reason for this was the need to file flight plans to the aviation authorities many hours before take-off. Decisions therefore had to rely on sometimes inaccurate forecasts. Still, the campaign successfully covered two polar low events. The first of these took place during 3–4 March 2008 over the Norwegian Sea, as will now be described.

In the days leading up to 3 March, available numerical weather prediction (NWP) models suggested that a polar low would develop over the Norwegian Sea (Figure 1). After carefully analysing NWP forecasts and satellite images, two flights were planned to be launched on 3 March. The first flight that started at 1000 UTC dropped 20 dropsondes between this time and 1300 UTC, intending to capture the polar low prior to the cyclogenesis stage of its development (Figure 2(c), below). After a quick refuelling break at Andøya airport the second flight was launched at 1430 UTC the same day. During the three-hour flight the explosive cyclogenesis stage of the polar low was targeted using 14 dropsondes (Figure 2(d), below). Both flight missions returned to Andøya having successfully carried out their missions. The NWP models, boosted by the targeted observations in an area where normally very few observational data are available for the GTS (Irvine *et al.*, 2011), predicted that the polar low would reach the mature stage early on 4 March. The third flight was launched at 1000 UTC on 4 March lasting about three hours. Twenty dropsondes successfully measured the mature structure of the polar low (Figure 2(f), below) before it dissolved as it made landfall at the coast of Norway ( $64^{\circ}\text{N}$ ,  $10^{\circ}\text{E}$ ) later that day.

The dropsondes used in the campaign are part of the US National Center for Atmospheric Research Global Positioning System (NCAR GPS) dropsonde system also known as AVAPS (Airborne Vertical Profiling System). The dropsondes measure pressure, temperature, humidity and horizontal wind, transmitting the data back to the aircraft. The accuracy of the soundings is  $\pm 1 \text{ hPa}$ ,  $\pm 0.1 \text{ K}$ ,  $\pm 5\%$  and  $\pm 0.5 \text{ m s}^{-1}$  for pressure, temperature, relative humidity and wind speed, respectively. The quality control of the data is done with the software package ASPEN (Martin,

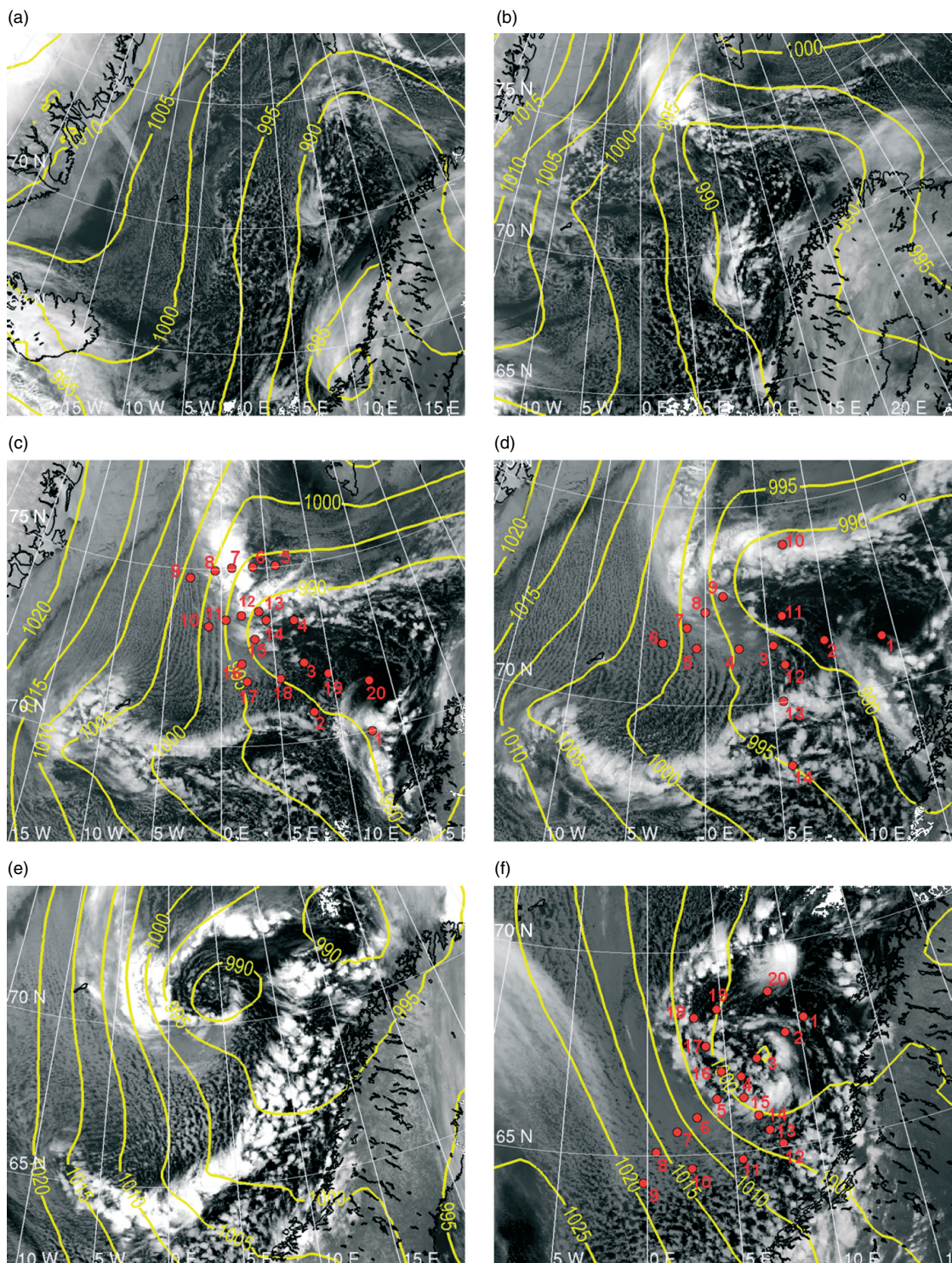


**Figure 2.** NOAA satellite images (infrared channel 4) documenting the temporal development of the polar low. Superimposed on the images is the mean-sea-level pressure (MSLP, yellow lines, hPa) from the HIRLAM analyses. (a) 1148 UTC on 2 March along with MSLP from the 1200 UTC analysis, (b) 0136 UTC 3 March with MSLP from the 0000 UTC analysis, (c) 1057 UTC 3 March with MSLP from the 1200 UTC analysis, (d) 1601 UTC 3 March with MSLP from the 3 hours forecast starting at 1200 UTC, (e) 0125 UTC 4 March with MSLP from the 0000 UTC analysis, and (f) 1128 UTC 4 March with MSLP from the 1200 UTC analysis. The red dots with numbers denote the dropsonde positions.

2007). In addition the vertical soundings were plotted and visually inspected to check that they looked realistic. The soundings typically start at around 350–400 hPa, or about 7.5 km above sea level, and terminate at the ocean surface. The time resolution is one observation every half second. This gives a vertical resolution of 5–6 m close to the surface and around 50 m at about 7 km height. After quality control, several observations in each sounding are often

discarded. This mostly affects the wind observations, which after quality control typically have more data gaps than the observations of temperature and humidity. In this study Matlab scripts were used to produce vertical cross-sections of potential temperature, relative humidity and wind speed by interpolation of dropsonde data from different flight legs (section 5). Only cross-sections of dropsonde data with good data coverage and sections we find useful for this study are

presented. Matlab scripts were also used to make horizontal plots of sea-level pressure (SLP), potential temperature and specific humidity at 920 hPa, by interpolating and extrapolating dropsonde data from all dropsondes during each flight (section 5). Similar horizontal plots were also made of the variable  $SST - T500$  hPa, which is the sea-surface temperature ( $SST$ ) minus the temperature at 500 hPa. The vertical sensible heat ( $SH$ ) and latent heat ( $LH$ ) fluxes were calculated using bulk formulae, where we have assumed (Hartmann, 1994) that the surface fluxes are proportional to the mean wind speed roughly at 10 m height ( $U_r$ ).

$$SH = c_p \rho C_{DH} U_r (T_s - T_a(Z_r)) \quad (1)$$

$$LH = L \rho C_{DE} U_r (q_s - q_a(Z_r)) \quad (2)$$

In the bulk aerodynamic formulae,  $\rho$  (1.225 kg m $^{-3}$ ) is the air density,  $c_p$  (1004 m $^{-2}$  s $^{-2}$  K $^{-1}$ ) is specific heat at constant pressure, and  $C_{DH}$  ( $1.14 \times 10^{-3}$ ) and  $C_{DE}$  ( $1.2 \times 10^{-3}$ ) are aerodynamic transfer coefficients for temperature and humidity, respectively. In our case,  $SST$  from the HIRLAM model (Figure 1) was used as surface temperature ( $T_s$ ), while specific humidity,  $q_a$ , and temperature,  $T_a$  were extracted from dropsonde data roughly at 10 m height. The specific humidity at the surface ( $q_s$ ), was calculated using the simplified equation of saturated specific humidity (Rogers and Yau, 1989)

$$q_s \approx \varepsilon \frac{e_s}{p}, \quad (3)$$

where  $\varepsilon$  is 0.62,  $p$  is surface pressure extracted from dropsonde data and  $e_s$ , which is the saturated partial pressure of the water vapour, was calculated using the empirical formula (Bolton, 1980):

$$e_s(T) = 6.112 \exp \left( \frac{17.67T}{T + 243.5} \right), \quad (4)$$

where  $SST$  was used as  $T$  in °C.

For dropsondes 9 and 10 of the first flight (Figure 2(c)) and dropsondes 1, 11, 13 and 16 of the third flight (Figure 2(f)), wind speed at 10 m height was estimated by extracting wind speed at about 50 m height and assuming a logarithmic wind profile. Because of coarse data coverage during the second flight on 3 March, only horizontal plots made of dropsonde data from the first flight mission on 3 March and the third flight mission which took place on 4 March will be presented.

### 3. Synoptic overview

The evolution of the synoptic conditions leading to the polar low development is presented in this section using infrared satellite images, as well as HIRLAM analysis and forecast products at 20 km horizontal grid spacing.

Figure 2(a) shows a satellite image valid at 1148 UTC on 2 March 2008. A synoptic-scale low moves eastward across the Norwegian Sea during the early hours of 2 March 2008 and weakens (980 hPa) at about 64°N, 10°E. The cyclonic flow associated with the low has advected relatively warm moist air toward the coast of northern Norway and further toward Svalbard, while an outbreak of Arctic air is initiated in the Fram Strait between Greenland and Svalbard (Figure 3(a)). During the next 12 hours a convergence zone develops along

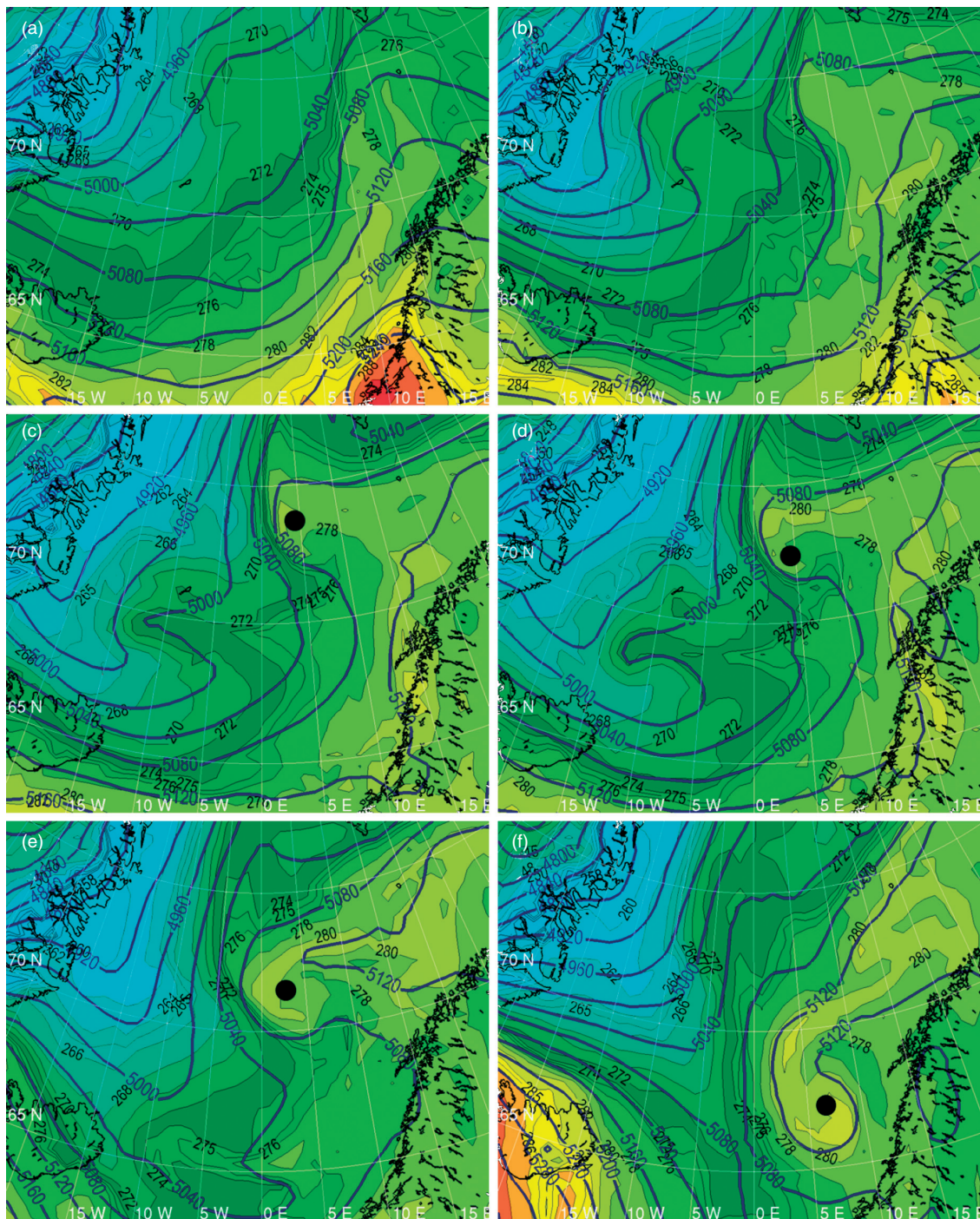
the 5°E meridian, stretching from the sea ice edge around 80°N to about 74°N (Figure 2(b)). The 1000–500 hPa thickness shows the baroclinic structure of the zone, with warm air to the east (Figure 3(a) and (b)) and a southerly thermal wind.

Figure 2(c) shows the infrared satellite image valid at 1237 UTC on 3 March, which is during the first flight that day. At this time the convergence zone has intensified and is now seen along the 0°E meridian, extending from the sea ice edge at about 80°N to about 72°N. Evidence of a northerly cold air outbreak west of the zone is seen as shallow cloud streets, parallel with the wind direction, developing downwind of the sea ice edge about 5° east of the coast of Greenland (70–80°N, 15–5°W, Figure 2(c)). A second convergence zone is now seen along 74°N latitude from the 0°E meridian to about 25°E (Figure 2(c)). This zone is caused by convergence of easterly winds north of the zone and milder, maritime air in the southeasterly winds south of the zone. A clear signature is found in equivalent potential temperature, while the large gradient of the 1000–500 hPa thickness shows the baroclinic structure of the two convergence zones discussed above (Figure 3(c)). Further downwind, more or less parallel to 70°N latitude, between 15°W and 5°E, another confluence zone is found, and we will hereafter refer to it as an Arctic front (Figure 2(c)). The equivalent potential temperature and 1000–500 hPa thickness show the Arctic front as a tongue of warm, humid air (Figure 3(c)), with cold air masses on both northern and southern sides.

At 1601 UTC, which is about halfway into the second flight mission on 3 March, a polar low is developing at the intersection between the two convergence zones, at about 73°N, 2°E (Figure 2(d)). Closer inspection of the satellite image in this area indicates the formation of an eye-like feature surrounded by cyclonic motion. The Arctic front discussed above has moved slightly south and is now found along 68°N latitude, with indications of a disturbance at its western edge. The development of the 1000–500 hPa thickness (Figure 3(b)–(d)) shows cold air masses that are wrapped around the polar low on its southern side, which is a manifestation of the baroclinic energy conversion as rising warm air and sinking cold air convert potential energy to kinetic energy of the developing disturbance.

During the night, the system intensified, and early on 4 March a satellite image valid at 0125 UTC shows a fully developed polar low with a clear eye-like structure centred at about 71°N, 3°E (Figure 2(e)). The mean-sea-level pressure (MSLP) from the 0000 UTC analysis shows a 988 hPa polar low with closed isobars, but the cyclonic cloud structure at the core of the polar low suggests that the model analysis places the polar low too far southeast. The Arctic front, with similar structure as discussed above, has moved southeastwards and is now found off the coast of northern Norway, curving westward along 65°N latitude to about 10°W (Figure 3(e)).

Figure 2(f) shows the satellite image valid at 1128 UTC on 4 March, which is about midway through the third flight mission. By now the polar low has moved south to about 67°N, 5°E and weakened to 995 hPa. However, according to scatterometer winds (not shown) the maximum surface wind speed west of the polar low has increased from about 15 to 20 m s $^{-1}$ . The centre of the polar low now consists of convective cells, with a spiral-like cloud band curving cyclonically to the north (Figure 2(f)). At this time the Arctic front has moved



**Figure 3.** Equivalent potential temperature at 850 hPa (colour shading with black labelled contours, every 2 K) and 1000–500 hPa thickness (blue contours, metres) from the HIRLAM analyses. (a) 1200 UTC on 2 March, (b) 0000 UTC 3 March, (c) 1200 UTC 3 March, (d) 3-hour forecast starting at 1200 UTC on 3 March, (e) 0000 UTC 4 March, and (f) 1200 UTC 4 March. The black dots show the approximate simulated positions of the polar low.

eastwards, reaching the coastline of Norway, and has started to dissipate (Figure 2(f)). The development of the equivalent potential temperature and the 1000–500 hPa thickness show signatures of a warm air advection process (Figure 3(d)–(f)). The weakened gradients of 1000–500 hPa thickness indicate that, in the mature stage of the polar low, baroclinic energy conversion has weakened (Figure 3(f)). The possible roles of condensational heating and surface energy fluxes will be discussed below. Satellite images and surface observations show that at about 1800 UTC the polar low dissipated as it made landfall over the coast of Norway ( $64^{\circ}\text{N}$ ,  $10^{\circ}\text{E}$ , not shown).

#### 4. Upper-level forcing

The simulated evolution of the upper-level PV structure on the 290 K isentropic surface from the HIRLAM analyses is shown in Figure 4. The usefulness of such charts is due to the fact that in the absence of frictional and diabatic effects, air parcels will flow along isentropic surfaces, and the PV of a given parcel is conserved (Hoskins *et al.*, 1985). Any alterations to the PV following the flow on this surface will be due to non-conservative effects such as diabatic heating.

At 1200 UTC on 2 March two upper-level PV (UPV) anomalies are clearly seen in Figure 4(a). A small-scale but

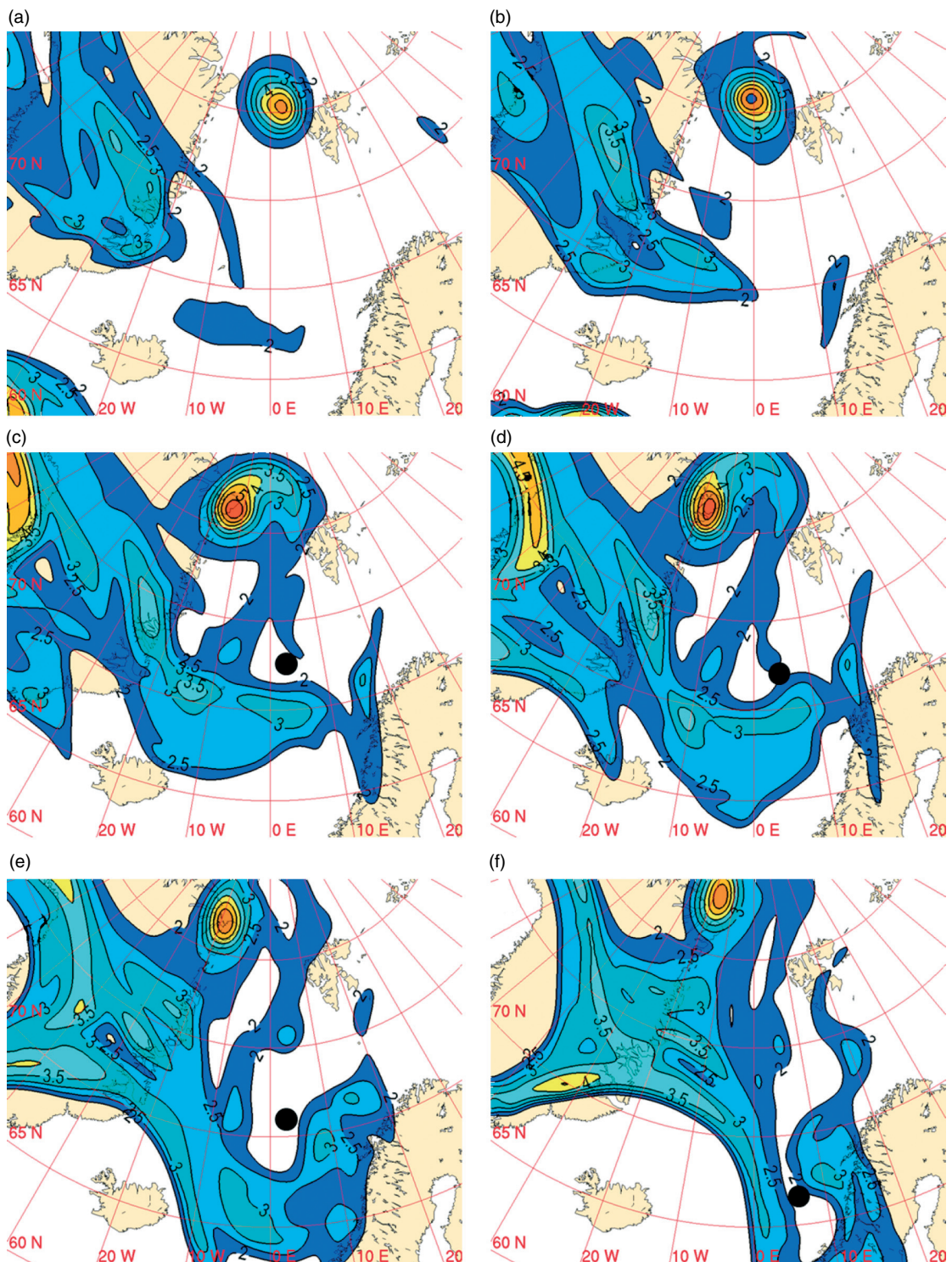


**Figure 4.** Isentropic potential vorticity at 290 K in PV units (colour shading) from the HIRLAM analyses valid at (a) 1200 UTC on 2 March, (b) 0000 UTC 3 March, (c) 1200 UTC 3 March, (d) 1800 UTC 3 March, (e) 0000 UTC 4 March, and (f) 1200 UTC 4 March. 1 PV unit (PVU) is equivalent to SI units  $1 \times 10^{-6} \text{ m}^2 \text{ s}^{-1} \text{ K} \text{ kg}^{-1}$ . The black dots show the approximate positions of the polar low.

intense (2–6 potential vorticity units (PVU)) UPV anomaly is located west of Svalbard at about 80°N, 3°E (Svalbard anomaly), while a large-scale tongue of high-PV air (2–3 PVU) is seen over Greenland centred around 75°N, 30°W (Greenland anomaly).

During the next 30 hours the Svalbard anomaly moves toward the west (Figure 4(b)–(d)), while the Greenland anomaly moves southeastward, reaching the area of cyclogenesis with especially high PV values (3 PVU) along 69°N latitude between 15°W and 10°E (Figure 4(b)–(d)).

A branch of high-PV air (2–2.5 PVU) along the 0°E meridian connects these two anomalies. We note that the polar low stays below the outer edge of the UPV anomaly (Figure 4(d)), and we suggest that this may be related to the condensational heating preventing the UPV anomaly from becoming vertically aligned with the surface polar low, as shown by Plant *et al.* (2003) and Bracegirdle and Gray (2009). Because of this, about midway into the third flight, at 1200 UTC 4 March, the high-PV air from the Greenland anomaly has wrapped around the polar low (Figure 4(e) and

(f)). The highest PV values (2–3 PVU) are seen northeast of the polar low, and to the west of it, along the 0°E meridian. The role of the UPV anomalies in initiating the polar low development will now be addressed.

#### 4.1. PV inversion

Given a PV distribution (Figure 4), balance conditions and suitable boundary conditions, the geopotential field, winds and temperature can be obtained by PV inversion (e.g. Hoskins *et al.*, 1985). The PV inversion system is based on Ertel's potential vorticity,  $q$ , which is given by

$$q = \frac{1}{\rho} \eta \cdot \nabla \theta, \quad (5)$$

where  $\rho$  is density,  $\eta$  is the absolute vorticity vector and  $\nabla \theta$  is the three-dimensional gradient of potential temperature. PV is expressed in PV units, defined as 1 PVU =  $10^{-6} \text{ m}^2 \text{s}^{-1} \text{ K kg}^{-1}$ . PV is modified by diabatic effects and friction according to

$$\frac{Dq}{Dt} \equiv \frac{\partial q}{\partial t} + \mathbf{u} \cdot \nabla q = \frac{1}{\rho} \eta \cdot \nabla \dot{\theta} + \frac{1}{\rho} \nabla \times \mathbf{F}_r \cdot \nabla \theta \quad (6)$$

where  $\mathbf{u}$  is the wind vector,  $\mathbf{F}_r$  is the friction force and  $\dot{\theta}$  denotes diabatic heating. Equation (6) shows that PV is conserved for a particle in adiabatic and inviscid flow. Now considering flow with small Rossby number (geostrophic scaling) and large Richardson number, by omitting friction, assuming hydrostatic flow and using isentropic coordinates, Eq. (6) becomes

$$\frac{\partial q}{\partial t} = -\mathbf{v}_\theta \cdot \nabla_\theta q + q^2 \frac{\partial}{\partial \theta} (\dot{\theta}/q) \quad (7)$$

where  $\mathbf{v}_\theta$  and  $\nabla_\theta$  are the horizontal wind vector and horizontal gradient operator, respectively, on a  $\theta$  (isentropic) surface. The second term on the right-hand side (RHS) of Eq. (7) shows that PV is enhanced (depleted) in the region below (above) a diabatic heating maximum (e.g. condensational heating). Hence a PV dipole is created with the connecting axis aligned along the absolute vorticity vector, as seen by the first term on the right-hand side of Eq. (6).

The PV inversion routine used in this investigation combines two inversion methods: adding the selected PV anomalies to the mean PV (average taken over e.g. 48 hours), referred to as 'addition to mean', and subtracting the PV anomalies from the total PV, described as 'subtraction from total' (Davis, 1992). This procedure yields almost the same result as the 'full linear' method of Davis and Emanuel (1991), according to Davis (1992). The procedure of defining PV anomalies is described in e.g. Kristjánsson *et al.* (1999). The inversion is based on Charney's balance condition (Charney, 1955) while horizontal boundary conditions are given by the hydrostatic relation. Vertical boundary conditions are given by the geopotential and stream function. This method allows the total flow to be obtained by adding the contributions from several PV anomalies, despite the nonlinearity of the Ertel PV (Kristjánsson *et al.*, 1999). The method has also been successfully used by Røsting and Kristjánsson (2006).

Three types of anomalies were defined in the PV inversion, following the conceptual model of polar low cyclogenesis

by Montgomery and Farrell (1992). The UPV anomaly was defined between 600 and 300 hPa. The lower left corner of the anomaly was set at about 62°N, 15°W while its upper right corner was at about 73°N, 20°E. Thus, this anomaly covered the Greenland anomaly and a part of the branch of high-PV air seen between this anomaly and the Svalbard anomaly (Figure 4(c)). The lower-level PV (LPV) anomaly was defined between 900 and 700 hPa, while the surface- $\Theta$  anomaly was defined at 950 hPa. No negative upper-level PV anomalies are presented since they were not found to be qualitatively important for the polar low development. By inverting the PV field the contribution from each PV anomaly to the atmospheric flow can be quantified. In our case the effects of the UPV, LPV and surface- $\Theta$  anomalies on the polar low circulation are analysed by comparing the magnitude of geopotential height contributions at 900 hPa.

The evolution of the contributions from different anomaly types to the 900 hPa height (i.e. polar low) is shown in Figure 5. With time the UPV anomaly shows increased effect at 900 hPa, reaching a peak value of  $-158 \text{ m}$  at 1800 UTC on 3 March as the polar low reached its mature stage, corresponding to about  $-20 \text{ hPa}$ . Subsequently, a rather rapid weakening of upper-level forcing with time is found. Both the surface- $\Theta$  anomaly and the LPV anomaly contributed to a deepening of the polar low ( $-40 \text{ m}$  and  $-50 \text{ m}$ , respectively) during the polar low cyclogenesis, but had gradually less effect as the polar low matured. The figure thus indicates that the high-PV air from the UPV anomaly has a strong influence on the circulation at lower atmospheric levels during the initiation of the polar low (Figure 5).

For completeness we carried out two PV inversion sensitivity experiments on the high-PV air from the UPV anomaly valid at 1200 UTC on 3 March. First, we increased the PV by 0.5 PVU between 600 and 300 hPa. This resulted in a further deepening of  $-40 \text{ m}$  (geopotential height) at the 900 hPa level. In the second experiment we reduced the PV by 0.5–2 PVU at different levels, with the largest reduction at the highest level and the smallest reduction in the two lowest levels (500 and 600 hPa, respectively). The UPV anomaly then reduced its effect on the surface circulation to  $-30 \text{ m}$  (geopotential height), which is a reduction of 100 m (Figure 5). Therefore, it is clear that the polar low development is very sensitive to the influence of the UPV anomaly. A PV inversion was also carried out on the branch of high-PV air seen between the Greenland and Svalbard anomalies at 1200 UTC on 3 March (Figure 4(c)). The results showed that this high-PV air had a deepening effect of  $-40 \text{ m}$  (geopotential height) at 900 hPa. Thus, this PV feature contributes much less to the polar low development than the Greenland anomaly does. In that sense, our results differ from those of Bracegirdle and Gray (2009), who carried out a PV inversion on high-PV air that phase-locked with a polar low over the Norwegian Sea. Their results showed that upper-level forcing initiated the polar low, but as the polar low matured, the LPV anomaly had the largest effect on the deepening of the polar low.

## 5. Structure of the polar low

### 5.1. Flight 1: Initiation of the cyclogenesis stage

The first flight took off at 1000 UTC on 3 March and lasted for about three hours, releasing 20 dropsondes in more or



**Figure 5.** The time (hour/day) evolution of the magnitude of geopotential height perturbations (metres) at 900 hPa attributable to the UPV anomaly (blue line), the LPV anomaly (red), and the surface- $\Theta$  anomaly (green). PV Inversions are calculated at six-hour intervals through the simulated polar low using HIRLAM analyses. The lower left corner of the UPV anomaly was at about 65°N, 10°W while its upper right corner was 70°N, 20°E. The UPV anomaly was defined between 600 and 300 hPa, the LPV anomaly between 900 and 700 hPa, and the surface- $\Theta$  anomaly at 950 hPa.

less five straight flight legs (Figure 2(c)). These dropsondes probed the polar low prior to the cyclogenesis stage. During the first flight the polar low position was relatively stationary.

### 5.1.1. Horizontal structure

In this subsection the horizontal structure of the initial stage of the polar low is analysed. Figures 6(a), 6(b), 6(c) and 6(d) show SLP, SST-T500 hPa, potential temperature and specific humidity at 920 hPa from the first flight mission, respectively. We take the 920 hPa surface to represent the upper part of the planetary boundary layer (PBL). According to Figure 6(a) the HIRLAM analysis underestimated the polar low intensity by 2 hPa (Figure 2(c)), and placed the polar low about 1° too far east. However, the simulated pressure gradients (Figure 2(c)) fit rather well with observations (Figure 6(a)). A parameter that has been regarded as a key factor in predicting atmospheric conditions favourable for polar low developments is the temperature difference between the sea surface and 500 hPa (SST-T500 hPa: Noer and Ovhed, 2003; Zahn and von Storch, 2008). For instance, at the Norwegian Meteorological Institute an SST-T500 hPa threshold of 43°C is used in forecasting polar low developments (G. Noer, personal communication). Blechschmidt *et al.* (2009) analysed 90 polar lows in the Nordic Seas over a two-year period and found typical SST-T500 hPa values of 48°C, but values as low as 40°C were not uncommon. As seen in Figure 6(b) this parameter has values of 45°C in the area of polar low cyclogenesis, in agreement with the discussion above. The influence of the SST on the SST-T500 hPa parameter is clearly seen in the section (Figure 6(b)), where SST values range from about -0.5°C in the northwest corner to about +5°C in the southwest corner (not shown), which results in rather low values of SST-T500 hPa northwest of the polar low. The tongue of lower SST-T500 hPa seen along the 8°E meridian (Figure 6(b)) is caused by warm air at upper levels in dropsonde 3 (not shown). The section

of potential temperature shows that relatively warm air (273 K) is found at the area of polar low formation, and also further north (Figure 6(c)), while a signature of the cold air outbreak is seen west of the polar low (Figure 2(c)), with potential temperature decreasing sharply westward (Figure 6(c)). The highest value of specific humidity is about 3.2 g kg<sup>-1</sup> (Figure 6(d)), and is found near the intersection between the two convergence zones discussed above (Figure 1(c)). Further west of this zone the specific humidity decreases (Figure 6(d)) along with the potential temperature (Figure 6(c)). As seen in Figure 6(e), maximum latent heat fluxes ( $\sim 170$  W m<sup>-2</sup>) are found at about 3°E, in an area where also maximum pressure gradients (i.e. surface wind speed) are seen (Figure 6(a)). The maximum sensible heat fluxes of about 200 W m<sup>-2</sup> are found somewhat further west, at about 1°E (Figure 6(f)). The relatively calm area (i.e. weak pressure gradients, Figure 6(a)) east and north of the developing polar low exhibits weak surface energy fluxes (Figure 6(e) and (f)).

### 5.1.2. Vertical structure

According to the satellite images the third flight leg, dropsondes 10–13 (Figure 2(c)), made a section (black dashed line, Figure 6(a)) through the area where polar low cyclogenesis took place. Figures 7(a)–(c) show southwest–northeast oriented cross-sections of potential temperature, relative humidity (RH) and wind speed based on these dropsondes. The intersection between the two convergence zones discussed above (Figure 2(c)) with a cold air outbreak to the west is seen as a shallow front that is most pronounced below 800 hPa (Figure 7(a)). Above 800 hPa the horizontal gradients of potential temperature are weak, confirming the very shallow baroclinic nature of the frontal structure so evident in Figure 6(c). The large vertical gradient of potential temperature at 450 hPa indicates the height of the tropopause (Figure 7(a)). The plot of relative humidity shows RH values above 70% reaching up to the tropopause

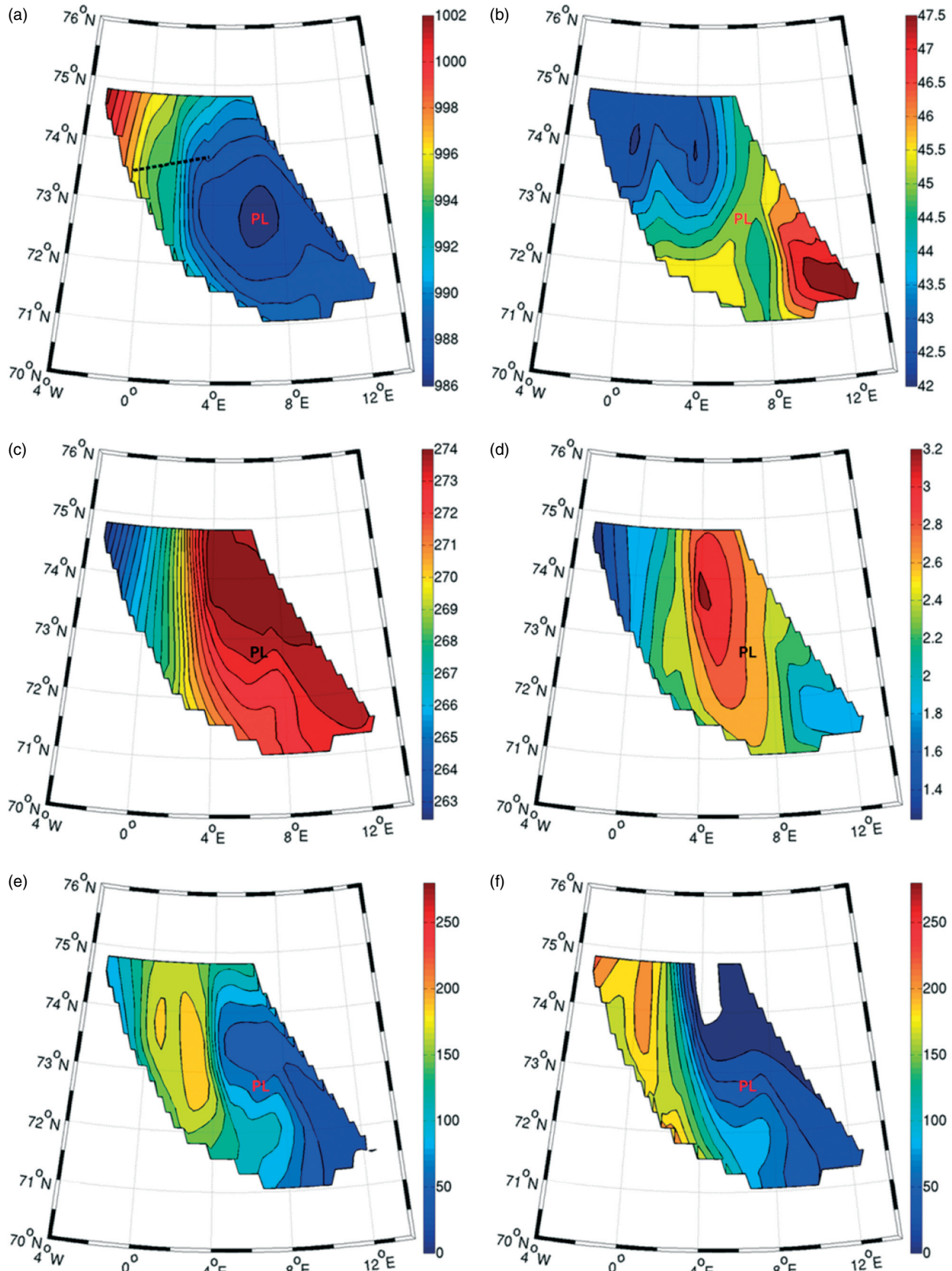


**Figure 6.** (a) Sea-level pressure (hPa, colour shading with black contours), (b) sea-surface temperature minus 500 hPa temperature (K, colour shading with black contours), (c) potential temperature (K, colour shading with black contours) at 920 hPa, (d) specific humidity ( $\text{g kg}^{-1}$ , colour shading with black contours) at 920 hPa, (e) latent heat flux at the surface ( $\text{W m}^{-2}$ , colour shading with black contours) based on bulk formulae, and (f) sensible heat flux at the surface ( $\text{W m}^{-2}$ , colour shading with black contours) based on bulk formulae. The plots were made by extrapolating and interpolating data from the 20 dropsondes taken during the first flight mission on 3 March (Figure 2(c)). The SSTs were extracted from the HIRLAM analyses. The polar low position is marked as PL. The black dashed line in (a) indicates the position of the cross-sections presented in Figure 7.

(Figure 7(b)), indicating the height of the clouds probed by the dropsondes (Figure 2(c)). The horizontal tongue of dry air at about 600 hPa on the right side of the figure is most likely due to sideways intrusion of dry air. The second flight leg (dropsondes 5–9) made a section through the same convergence zone about 150 km further north (Figure 2(c)). As shown in Kristjánsson *et al.* (2011), cross-sections from these dropsondes showed similar frontal structure as seen in Figure 7(a), but the zone was sharper and reached up to about 700 hPa.

Figure 7(c) shows a cross-section of wind speed and wind direction at this time. A maximum wind speed of  $26 \text{ m s}^{-1}$  is observed in dropsonde 11 at about 920 hPa height (Figure 7(c)), which is on the northwest side of the developing polar low (Figure 2(c)). As indicated by the cloud structure in the satellite observations (Figure 2(c)), the cold air outbreak west of the convergence zone is dominated by northerly winds (Figure 7(c)). As seen in Kristjánsson *et al.* (2011), a similar low-level northerly wind jet was found at the convergence zone probed during the second flight leg (dropsondes 5–9, Figure 2(c)). Due to the southerly thermal wind seen in this polar low case (thickness lines in Figure 3(c)) and the northerly low-level jet, the wind is expected to decrease with height above the PBL. Such reversed wind shear is common for many polar lows in the Nordic Seas (Kolstad, 2006). In the PBL however, friction reduces the wind speed towards the ground, resulting in a low-level jet somewhere in the upper part of the PBL. At the intersection of the two convergence zones, two upper-level jets are apparent (Figure 7(c)). The northeasterly wind jet ( $\sim 16 \text{ m s}^{-1}$ ) seen at 550 hPa in dropsonde 11 is most likely related to the tropopause fold seen at this location (Figure 7(a)), while the second northeasterly wind jet ( $\sim 18 \text{ m s}^{-1}$ ), seen at 700 hPa in dropsonde 12, is most likely a frontal jet.

## 5.2. Flight 2: Cyclogenesis stage

The second flight on 3 March took off at 1430 UTC and lasted for three hours, dropping 14 sondes in three straight flight legs (Figure 2(d)), that observed the cyclogenesis stage of the polar low. During this flight several dropsonde data contained errors or gaps of missing data, which limits the numbers of cross-sections useful for this study. For the same reason, no horizontal plots are presented from this flight.

### 5.2.1. Vertical structure

During the second flight leg, dropsondes 6–10 made a southwest–northeast oriented section near the centre of the developing polar low (Figure 2(d)). Figures 8(a)–(c) show cross-sections of potential temperature, relative humidity and wind speed based on the dropsondes. In the lower levels of Figure 8(a) we recognize the shallow frontal structure discussed above. However, the frontal structure is sharper than in Figure 7 because the dropsondes captured the cold air outbreak southwest of the developing polar low, as well as its warmer and calmer central part (Figures 2(d) and 3(d)).

The tropopause is found at about the same height ( $\sim 450 \text{ hPa}$ ) as in the first flight. A striking feature at higher levels is the downfolding of the potential temperature near the centre of the developing polar low (dropsonde 8). We suggest that this may be caused by intrusion of stratospheric dry air with higher potential

temperature than its surroundings, and this is supported by the RH in dropsonde 8 (Figure 8(b)). Such upper troposphere downfolding can be an indication of a UPV anomaly (Hoskins *et al.*, 1985). On both sides of the UPV anomaly, RH values above 60% reach up to about 600 hPa (Figure 8(b)), indicating the depth of the moist convection near the area of cyclogenesis (Figure 2(d)). Based on the above discussion we conclude that initially the polar low developed in a low-level baroclinic environment under the influence of upper-level PV forcing (e.g. Montgomery and Farrell, 1992). It should be mentioned that also in dropsonde 3, released during the first flight, both RH and potential temperature showed evidence of a UPV anomaly (not shown). This suggests that UPV forcing was already taking place at 1200 UTC, supporting the results of Figure 5, even if this was not evident in the cross-sections of Figure 7.

The cross-section of wind speed (Figure 8(c)) shows the reversed-shear nature of the developing polar low, with a north-northwesterly low-level jet with wind speed reaching up to  $24 \text{ m s}^{-1}$  confined below 800 hPa (at 50–200 km distance in Figure 8(c)).

## 5.3. Flight 3: Mature polar low

On 4 March the third and last mission into the polar low took off at 1000 UTC, lasting about three hours and dropping a total of 20 dropsondes that probed the mature stage of the polar low (Figure 2(f)). It should be mentioned that the polar low moved southward at about  $25 \text{ km h}^{-1}$  during the third flight.

### 5.3.1. Horizontal structure

Figures 9(a), 9(b), 9(c) and 9(d) show the SLP,  $SST-T500 \text{ hPa}$ , potential temperature and specific humidity from the 20 dropsonde observations, approximately 24 hours later than the first flight (Figure 6). In the polar low mature stage its position, central pressure (995 hPa) and the pressure gradients in the HIRLAM analyses agree well with dropsonde observations throughout (Figure 2(f) vs. 9(a), respectively). It is notable that despite the polar low having weakened by almost 9 hPa during the preceding 24 hours the pressure gradients in its vicinity have sharpened (Figure 9(a) vs. 6(a), respectively), causing the intensifying wind speed in the mature stage to increase (see below). By now  $SST-T500 \text{ hPa}$  has increased to about  $49.5^\circ\text{C}$  both southwest and southeast of the polar low (Figure 9(b)), exceeding by  $1.5^\circ\text{C}$  the typical value for polar low developments in the Nordic Seas found by Blechschmidt *et al.* (2009). At this stage the polar low is secluded with a warm core isolated from the surrounding colder air (Figure 9(c)), and at the eye-like structure of the polar low (Figure 2(f)) the temperature is now 276 K at this level, an increase of about 3 K during the last 24 hours (Figure 6(c) vs. Figure 9(c), respectively). The maximum temperature (Figure 9(c)) is found below the spiral-like cloud band curving to the north on the southern and western edges of the eye-like structure of the polar low (Figure 2(f)), in an area where increased maximum specific humidity of  $3.7 \text{ g kg}^{-1}$  is also found (Figure 9(d)).

During the last 24 hours the wind speed southwest of the polar low has intensified (see below), which most likely explains the increased maximum latent heat ( $300 \text{ W m}^{-2}$ ) and sensible heat ( $280 \text{ W m}^{-2}$ ) fluxes seen southwest of

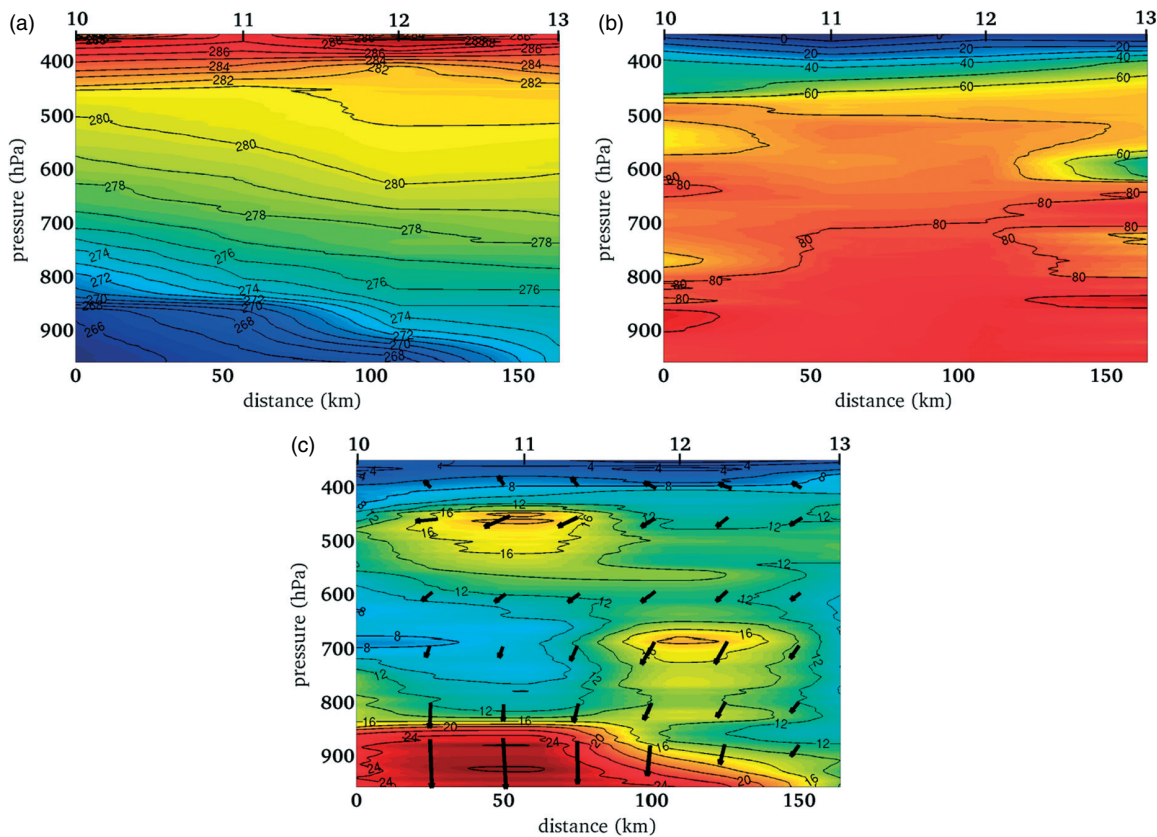


**Figure 7.** Cross-sections of (a) potential temperature (K), (b) relative humidity (%), and (c) wind speed ( $\text{m s}^{-1}$ ) from dropsondes 10–13 from the first flight mission on 3 March (Figure 2(c)). The arrows show the direction of the horizontal wind at different levels, with the length of the arrow being proportional to the wind speed. The dropsonde positions are marked as black bars with numbers on top of the figures. The x-axis shows the horizontal distance along the section, where zero is at west.

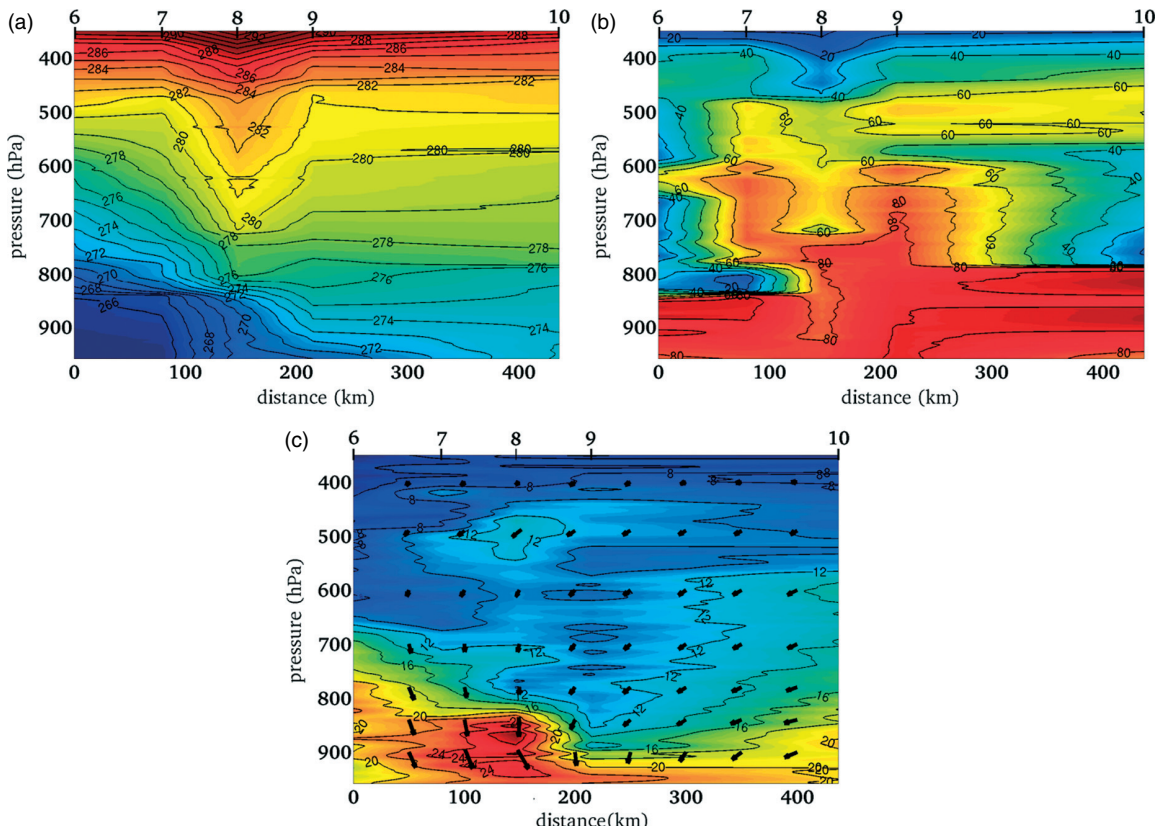


**Figure 8.** Cross-sections of (a) potential temperature (K), (b) relative humidity (%), and (c) wind speed ( $\text{m s}^{-1}$ ) of dropsondes 6–10 from the second flight mission on 3 March (Figure 2(d)). The arrows show the direction of the horizontal wind at different levels, with the length of the arrow being proportional to the wind speed. The dropsonde positions are marked as black bars with numbers on top of the figure. The x-axis shows the horizontal distance along the section, where zero is at southwest.

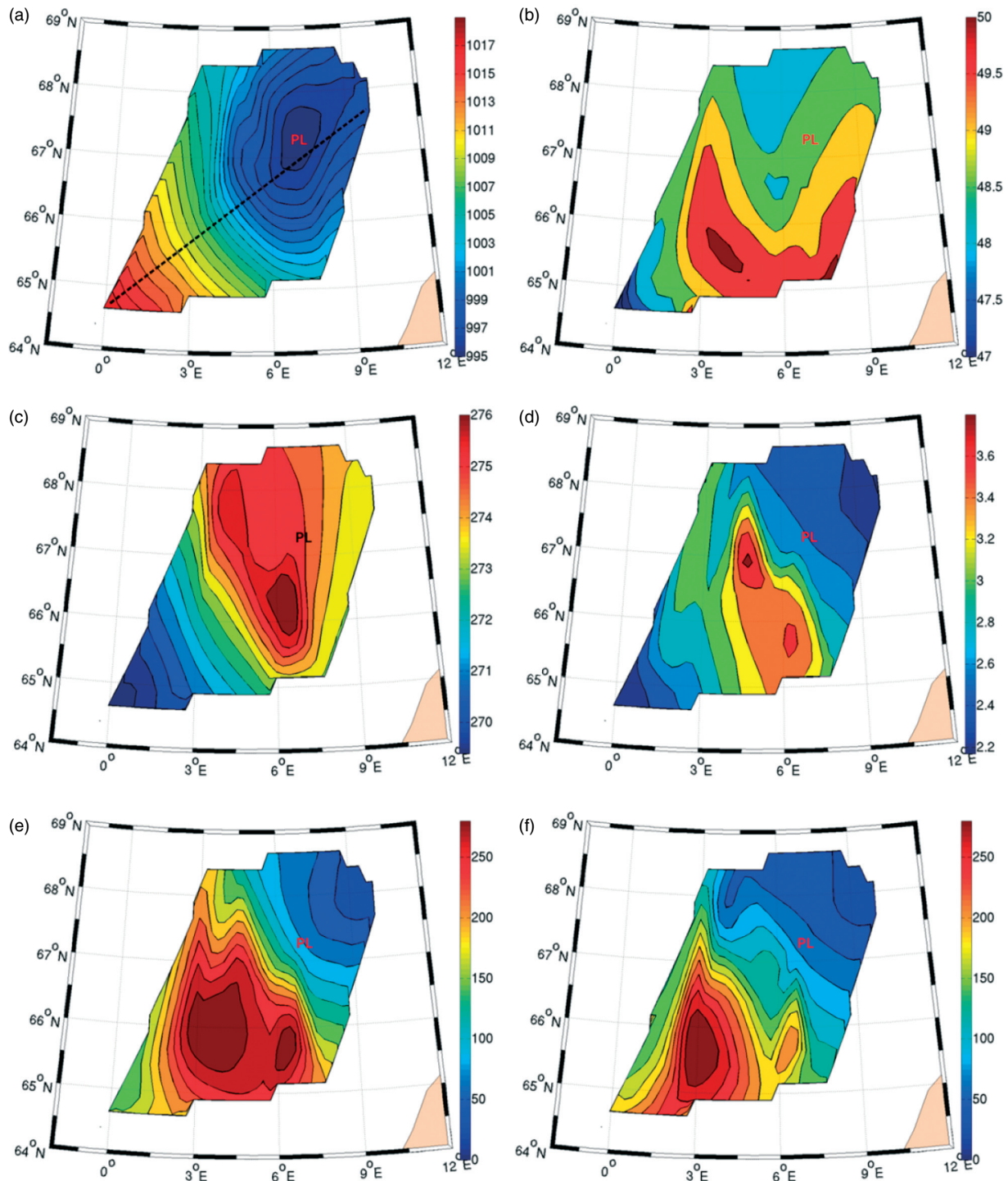


**Figure 9.** (a) Sea-level pressure (hPa, colour shading with black contours), (b) sea-surface temperature minus 500 hPa temperature (K, colour shading with black contours), (c) potential temperature (K, colour shading with black contours) at 920 hPa, (d) specific humidity ( $\text{g kg}^{-1}$ , colour shading with black contours) at 920 hPa, (e) latent heat flux at the surface ( $\text{W m}^{-2}$ , colour shading with black contours) and (f) sensible heat flux at the surface ( $\text{W m}^{-2}$ , colour shading with black contours), based on bulk formulae. The plots were made by extrapolating and interpolating data from the 20 dropsondes taken during the third flight mission (Figure 2(f)) which took place on 4 March. SST was extracted from the HIRLAM analyses. The polar low position is marked as PL. The black dashed line in (a) indicates the position of the cross-sections presented in Figure 10. Note the differences in the colour bar (a)–(d) compared to Figure 5.

the polar low (Figure 9(e) and (f), respectively). Thus, we attribute the increase in temperature and moisture in the PBL during the last 24 hours, at least to a large extent, to the increased surface fluxes of latent and sensible heat during this period. The impact of wind-induced surface heat exchange (WISHE) was investigated by Emanuel and Rotunno (1989), applying the air-sea interaction theory of Emanuel (1986) to polar lows. They showed that warming and moistening

of the planetary boundary layer, as seen in our case, may indeed be an important contribution to the energetics of polar lows. Shapiro *et al.* (1987) carried out the first-ever research aircraft measurements within a polar low over the Norwegian Sea during the Arctic Cyclone Expedition (27 February 1984). They estimated surface energy fluxes based on aircraft measurements at 300 m height above sea level. For that polar low, maximum latent heat and sensible heat

fluxes were each about  $500 \text{ W m}^{-2}$ , i.e. almost twice as high as in our case. Artificially setting the wind speed equal to the maximum wind speed ( $35 \text{ m s}^{-1}$ ) observed by Shapiro *et al.* (1987), our polar low would have had maximum latent heat fluxes of about  $500 \text{ W m}^{-2}$  and sensible heat fluxes of about  $430 \text{ W m}^{-2}$ , indicating that the lower values in our case are mainly caused by the weaker winds at low levels.

### 5.3.2. Vertical structure (flight leg 1)

According to the satellite images the first flight leg, dropsondes 1–9 (Figure 2(f)), made a section (black dashed line, Figure 6(a)) near the polar low centre.

Figure 10(a), (c) and (e) show northeast–southwest oriented cross-sections of potential temperature, relative humidity and wind speed based on these dropsondes. Below 700 hPa the remains of the frontal structure, with a cold air outbreak on its southwest side, discussed earlier, are seen on the left side of the section (Figure 10(a)). The large vertical gradient of potential temperature shows that the tropopause is located at about 450–500 hPa (Figure 10(a)). The now weaker horizontal gradients of potential temperature indicate that low-level baroclinic energy conversion has weakened (Figure 7(a) vs. Figure 10(a)). This is consistent with the weaker gradients of 1000–500 hPa thickness seen in the HIRLAM analyses (Figure 3(f)). The polar low now has a warm core (274 K), which is about 5 K warmer than the cold air outbreak seen on the southwest side of the section (Figure 10(a)). In the area of dropsondes 6–9 a sharp inversion is found just below 800 hPa (Figure 10(a)), and the RH (Figure 10(c)) indicates a trapping of the moisture below the inversion with dry air above. The satellite images (Figure 2(f)) indicate shallow stratiform clouds at lower levels in this region. By contrast, the convective towers seen in the cloud band curving to the north (Figure 2(f)) more or less penetrate the whole troposphere, and relative humidities above 60% are observed all the way up to 500 hPa (dropsonde 5 in Figure 10(c)). A very interesting feature in Figure 10(c) is the dry upper-level air with relative humidities of 20% reaching down to 700 hPa near the centre of the cyclone below dropsonde 4, which is near the centre of the polar low (Figure 2(f)). Linking this to the downfolding of the potential temperature surfaces at the same location found in Figure 10(a), we interpret this as evidence of an intrusion of dry stratospheric air. This is similar to the feature that was observed during the second flight on 3 March (sonde 8 in Figure 8). The area of highest wind speed in dropsondes 5–6 (Figure 10(e)), found between the UPV anomaly and the polar low, is viewed as evidence of a phase lock and mutual interaction between the low-level circulation and the UPV anomaly (Montgomery and Farrell 1992), as is evident by the much deeper circulation in Figure 10(e) than in Figure 7(c). Thus, we suggest that upper-level forcing may also contribute to surface development in the later stages of the observed polar low, which is consistent with the result from the PV inversion (section 4).

### 5.3.3. Vertical structure (flight leg 3)

The third flight leg, which consisted of dropsondes 12–18, made a straight transect that passed through the polar low from southeast to northwest (Figure 2(f)). Figures 10(b), (d) and (f) show southeast–northwest oriented cross-sections of potential temperature, relative humidity and

wind speed based on these dropsondes, respectively. The downfolding of potential temperature (dropsondes 14–16, Figure 10(b)) is similar to what was seen in dropsondes 3–5 above (Figure 10(a)). Likewise, the plot of RH confirms a dry intrusion in dropsonde 15 (Figure 10(d)), similar to what was seen in nearby dropsonde 4 (Figure 10(c)). Thus, because of the short horizontal distance between dropsondes 3–5 and 14–16 (Figure 2(f)) it is likely that they all show the manifestation of the same UPV anomaly. As indicated by the satellite images (Figure 2(f)) dropsonde 14 probed a deep moist cloud band located on the southern outer edge of the polar low eye-like structure. This feature is seen as RH values above 70% reaching up to about 550 hPa (Figure 10(d)), indicating deep convection. As shown by Figure 9(f) the highest wind speed is found on the southwestern side of the polar low centre (dropsondes 14–17), below the spiralling tail of convective clouds stretching to the north (Figure 2(f)). This part of the section shows northwesterly wind speed above  $20 \text{ m s}^{-1}$  throughout (Figure 10(f)). Similarly to what was seen in dropsonde 5 (Figure 10(e)), low-level jets appear in dropsondes 14 and 16 with maximum wind speed of about  $26\text{--}28 \text{ m s}^{-1}$  (Figure 10(f)). The slightly weaker wind speed seen in dropsonde 15 may be explained by the dropsonde hitting the central structure of the polar low, which according to the nearby dropsonde 4 (Figure 10(e)) is fairly calm.

## 6. Summary and conclusions

The main goal of this study is to document the three-dimensional structure and physical properties of a polar low that evolved during 3–4 March 2008 over the Norwegian Sea. This has been done by analysis of dropsonde data from the Norwegian IPY-THORPEX research aircraft campaign, combined with analyses and forecast products of the operational Norwegian NWP model HIRLAM. The observations, mainly by dropsondes from three separate flights, managed for the first time in history to measure the full lifetime of a polar low development. Observations like this are not only important to improve our knowledge about polar lows but also to serve as a reference for model validations in numerical studies (e.g. McInnes *et al.*, 2011).

During the polar low development the temperature difference between the sea surface and temperature at 500 hPa ( $\text{SST} - T_{500} \text{ hPa}$ ) was about  $45\text{--}50^\circ\text{C}$ . Such high values, which are caused by cold air outbreaks over relative warm seas, represent favourable conditions for polar low development (Kolstad, 2006; Kolstad and Bracegirdle, 2008). In Blechschmidt *et al.* (2009) a typical value of 48 K was found for polar low development over the Nordic Seas, in agreement with our observations.

Cross-sections of dropsonde data from the first and second flight missions showed strong horizontal gradients of potential temperature below 700 hPa. As the polar low matured the horizontal gradients weakened, which suggests that low-level baroclinic energy conversion was important during the cyclogenesis stage of the polar low. The HIRLAM analyses showed that high-UPV air found over Greenland, about 24 hours prior to the polar low development, moved eastward and became wrapped around the polar low during its mature stage. An inversion of this UPV anomaly showed that upper-level PV forcing was important for the surface circulation throughout the polar low's lifetime, reaching a peak value of about  $-20 \text{ hPa}$  at 900 hPa as the polar low

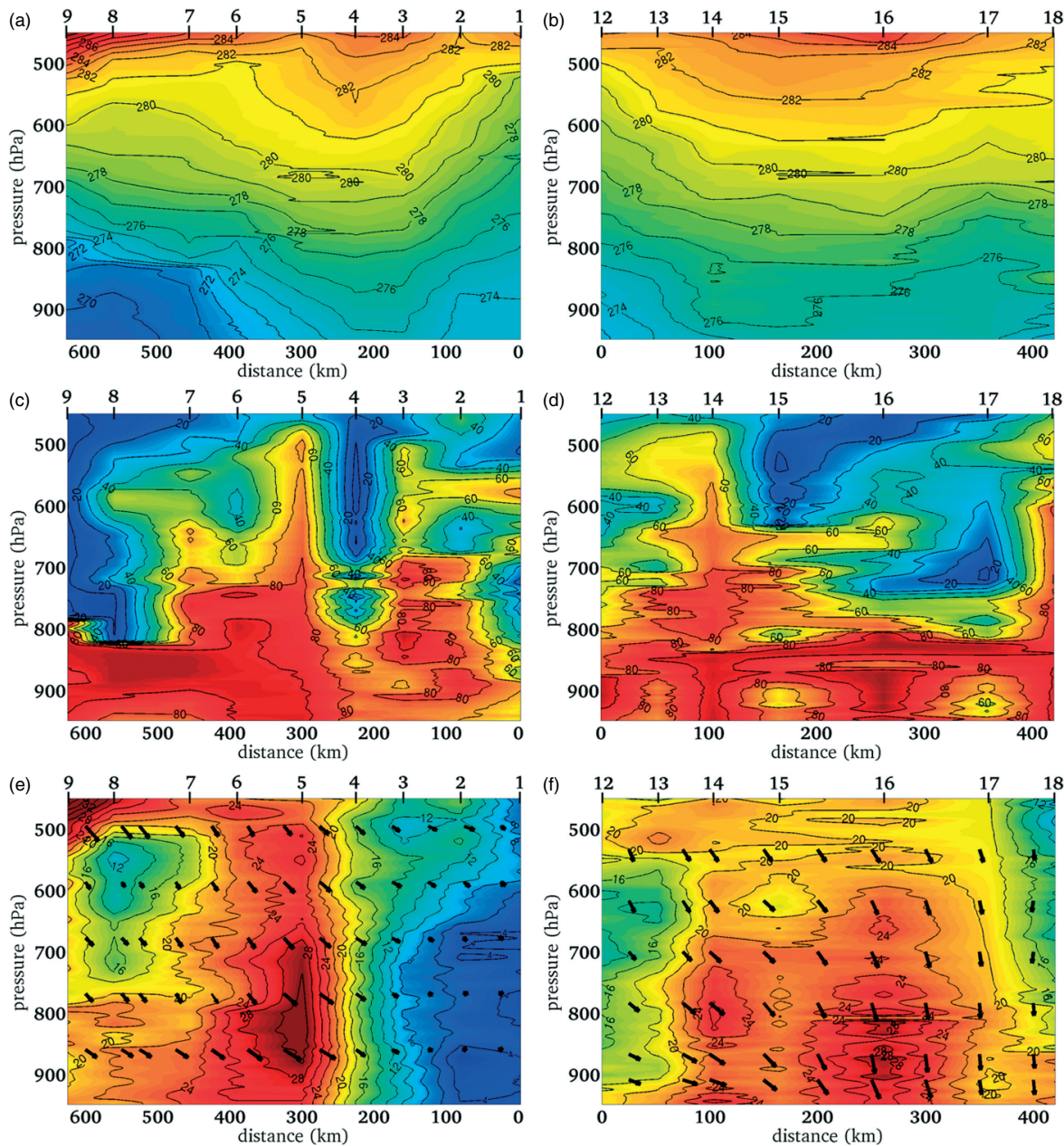


**Figure 10.** The left column shows cross-sections of (a) potential temperature (K), (c) relative humidity (%), and (e) wind speed ( $\text{m s}^{-1}$ ) of dropsondes 1–9 from the third flight mission (Figure 2(f)), which took place on 4 March. The arrows show the direction of the horizontal wind at different levels. The dropsonde positions are marked as black bars with numbers on top of the figure. The x-axis shows the horizontal distance along the section, where zero is at northeast. The right column (b), (d) and (f) shows cross-sections of the same variables from dropsondes 12–18 from the same flight mission (Figure 1(f)), where the x-axis shows the horizontal distance along the section going from southeast (left) to northwest (right).

reached its mature stage. Initially the contributions from an LPV anomaly and a surface- $\Theta$  anomaly were each about one third of that from the UPV anomaly, but as the polar low matured they both had an insignificant effect on the development. Cross-sections of the dropsonde data showed evidence of a tropopause fold during the last two flights, which is likely a manifestation of upper-level forcing on the polar low (e.g. Hoskins *et al.*, 1985; Montgomery and Farrell, 1992) from the UPV anomaly. Based on clear evidence of tropopause folding in the dropsonde data and the results from the PV inversion, we conclude that a UPV anomaly interacted with low-level baroclinicity resulting in polar low cyclogenesis, in agreement with the scenario described in Grønås and Kvamstø (1995), but that upper-level PV forcing was also important during the mature stage of the polar low,

which differs from the findings of Bracegirdle and Gray (2009). Thus, the relative roles of upper-level, low-level and surface- $\Theta$  anomalies in inducing surface circulation may be quite different from case to case.

Sections of dropsonde data showed that the polar low circulation was confined below 700 hPa during the cyclogenesis stage, with a northerly jet with a maximum wind speed of about  $26 \text{ m s}^{-1}$ . In the mature stage the vertical extent of the circulation of the polar low reached up to tropopause height with wind speeds of about  $20 \text{ m s}^{-1}$ . A northwesterly low-level jet (750–900 hPa) with maximum wind speed of  $28\text{--}31 \text{ m s}^{-1}$  was observed on the western cold side of the polar low. As seen in previous aircraft-based observations of polar lows (Shapiro *et al.*, 1987; Brümmer *et al.*, 2009) our polar low developed a warm core that

was about 3 K warmer than the surrounding air masses. The dropsonde data showed that the moist towers at the eye-like structure of the polar low, which had RH values of 70%, reached up to the tropopause. This suggests that condensational heating has played an essential role in the polar low development. McInnes *et al.* (2011) carried out a sensitivity experiment on this polar low in which they reduced the condensational heating to 10% of original values using the UK Unified Model. This resulted in a much weaker polar low development, in agreement with our suggestions.

By comparing horizontal sections of dropsonde data at 920 hPa between 3 March and 4 March, an increase of maximum potential temperature of about 3 K and of specific humidity of about 0.5 g kg<sup>-1</sup> was observed at the western side of the polar low. In the same areas the low-level jet increased its maximum wind speed by about 4 m s<sup>-1</sup>. This most likely explains the increased surface energy fluxes seen during this 24-hour period, as latent heat fluxes increased by about 130 W m<sup>-2</sup> and sensible heat fluxes by about 80 W m<sup>-2</sup>. As seen in Craig and Gray (1996), surface energy fluxes may be an important contribution to the energetics of the polar lows. The role of surface energy fluxes for polar low development can best be answered through numerical sensitivity experiments, as in Føre *et al.* (2011), which is beyond the scope of this study.

## Acknowledgements

This study has received support from the Norwegian Research Council through the project 'THORPEX-IPY: Improved forecasting of adverse weather in the Arctic – present and future' (grant no. 175992). A special thanks to all the scientists at the Andøya Rocket Range during the IPY-THORPEX flight campaign as well as the DLR staff that successfully carried out the research aircraft measurements using the Falcon aircraft during the campaign. The first author wishes to thank Ole Vignes and Trygve Aspelin at The Norwegian Meteorological Institute for providing the HIRLAM analyses and for valuable discussions. The first author wishes particularly to thank Bjørn Egil Nygård and Øyvind Hodnebrog for support with Matlab and special thanks go to Gunnar Noer at the Norwegian Meteorological Institute for valuable discussion. To all my colleagues at MetOs, thanks for your motivating support and discussions.

## References

- Blechschmidt A-M, Bakan S, Graßl H. 2009. Large-scale atmospheric circulation patterns during polar low events over the Nordic seas. *J. Geophys. Res.* **114**: D06115, DOI: 10.1029/2008JD010865.
- Bolton D. 1980. The computation of equivalent potential temperature. *Mon. Weather Rev.* **108**: 1046–1053.
- Bracegirdle TJ, Gray SL. 2008. An objective climatology of the dynamical forcing of polar lows in the Nordic seas. *Int. J. Climatol.* **28**: 1903–1919.
- Bracegirdle TJ, Gray SL. 2009. The dynamics of a polar low assessed using potential vorticity inversion. *Q. J. R. Meteorol. Soc.* **135**: 880–893.
- Bresch JF, Reed RJ, Albright MD. 1997. A polar-low development over the Bering Sea: Analysis, numerical simulation, and sensitivity experiments. *Mon. Weather Rev.* **125**: 3109–3130.
- Brümmer B, Müller G, Noer G. 2009. A polar low pair over the Norwegian Sea. *Mon. Weather Rev.* **137**: 2559–2575.
- Charney J. 1955. The use of the primitive equations of motion in numerical prediction. *Tellus* **7**: 22–26.
- Craig GC, Gray SL. 1996. CISK or WISHE as the mechanism for tropical cyclone intensification. *J. Atmos. Sci.* **53**: 3528–3540.
- Davis CA. 1992. Piecewise potential vorticity inversion. *J. Atmos. Sci.* **49**: 1397–1411.
- Davis CA, Emanuel KA. 1991. Potential vorticity diagnostics of cyclogenesis. *Mon. Weather Rev.* **119**: 1929–1953.
- Douglas MW, Fedor LS, Shapiro MA. 1991. Polar low structure over the northern Gulf of Alaska based on research aircraft observations. *Mon. Weather Rev.* **119**: 32–54.
- Emanuel KA. 1986. An air–sea interaction theory for tropical cyclones. Part 1: Steady-state maintenance. *J. Atmos. Sci.* **43**: 585–605.
- Emanuel KA, Rotunno R. 1989. Polar lows as Arctic hurricanes. *Tellus* **41A**: 1–17.
- Føre I, Kristjánsson J, Kolstad E, Bracegirdle T, Røsting B, Saetra Ø. 2011. A 'hurricane-like' polar low fuelled by sensible heat flux: high-resolution numerical simulations. *Q. J. R. Meteorol. Soc.* (in press).
- Grønås S, Kvamstø NG. 1995. Numerical simulations of the synoptic conditions and development of Arctic outbreak polar lows. *Tellus* **47A**: 797–814.
- Hartmann DL. 1994. *Global Physical Climatology*. Academic Press.
- Hoskins BJ, McIntyre ME, Robertson AW. 1985. On the use and significance of isentropic potential vorticity maps. *Q. J. R. Meteorol. Soc.* **111**: 877–946.
- Irvine EA, Gray SL, Methven J. 2011. Targeted observations of a polar low in the Norwegian Sea. *Q. J. R. Meteorol. Soc.* **137**: 1688–1699, DOI: 10.1002/qj.914.
- Kolstad EW. 2006. A new climatology of favourable conditions for reverse-shear polar lows. *Tellus* **58A**: 344–354.
- Kolstad EW, Bracegirdle TJ. 2008. Marine cold-air outbreaks in the future: An assessment of IPCC AR4 model results for the Northern Hemisphere. *Clim. Dyn.* **30**: 871–885.
- Kristjánsson JE, Thorsteinsson S, Ulfarsson GF. 1999. Potential vorticity-based interpretation of the evolution of 'The Greenhouse Low', 2–3 February 1991. *Tellus* **51A**: 233–248.
- Kristjánsson JE, Barstad I, Aspelien T, Føre I, Hov Ø, Irvine E, Iversen T, Kolstad EW, Nordeng TE, McInnes H, Randriamampianina R, Saetra Ø, Shapiro M, Spengler T, Ólafsson H. 2011. The Norwegian IPY-THORPEX: Polar lows and Arctic fronts during the 2008 Andøya campaign. *Bull. Am. Meteorol. Soc.* (in press).
- Martin C. 2007. 'The ASPEN user manual.' Available from National Center for Atmospheric Research, Boulder, Colorado, USA, 61 pp.
- McInnes H, Kristiansen J, Kristjánsson JE, Schyberg H. 2011. The role of horizontal resolution for polar low simulations. *Q. J. R. Meteorol. Soc.* **137**: DOI: 10.1002/qj.849, this issue (in press).
- Montgomery MT, Farrell BF. 1992. Polar low dynamics. *J. Atmos. Sci.* **49**: 2484–2505.
- Noer G, Ovhed M. 2003. 'Forecasting of polar lows in the Norwegian and the Barents Sea.' *Proc. 9th Meeting of the EGS Polar Lows Working Group*. European Geophysical Society: Cambridge, UK.
- Plant RS, Craig GC, Gray SL. 2003. On a threefold classification of extratropical cyclogenesis. *Q. J. R. Meteorol. Soc.* **129**: 2989–3012.
- Rasmussen EA, Turner J (eds). 2003. *Polar Lows*. Cambridge University Press: Cambridge, UK.
- Rogers RR, Yau MK. 1989. *A Short Course in Cloud Physics*. 3<sup>rd</sup> edn. Butterworth Heinemann.
- Røsting B, Kristjánsson JE. 2006. Improving simulations of severe winter storms by initial modification of potential vorticity in sensitive regions. *Q. J. R. Meteorol. Soc.* **132**: 2625–2652.
- Shapiro MA, Fedor LS, Hampel T. 1987. Research aircraft measurements of a polar low over the Norwegian Sea. *Tellus* **39A**: 272–306.
- Turner J, Rasmussen EA, Røsting B. 2003. Forecasting of polar lows. *PP 501–574 in Polar Lows: Mesoscale Weather Systems in the Polar Regions*. Rasmussen EA, Turner J (eds). Cambridge University Press.
- Undén P, Rontu L, Järvinen H, Lynch P, Calvo J, Cats G, Cuxart J, Eerola K, Fortelius C, García-Moya JA, Jones C, Lenderlink G, McDonald A, McGrath R, Navascués B, Nielsen NW, Ødegaard V, Rodriguez E, Rummukainen M, Room R, Sattler K, Sass BH, Savijärvi H, Schreure BW, Sigg R, The H, Tijm A. 2002. 'HIRLAM-5 scientific documentation'. HIRLAM-5 Project, c/o Per Undén, SMHI, S-601 76 Norrköping, Sweden, 144 pp.
- Zahn M, von Storch H. 2008. A long-term climatology of North Atlantic polar lows, *Geophys. Res. Lett.* **35**: L22702, DOI: 10.1029/2008GL035769.